

New bounds on Lorentz violation from a composite pulse method in a trapped ion

Laura S. Dreissen^{1*}, Chih-Han Yeh¹, Henning A. Füst^{1,2}, Kai C. Grensemann¹ and Tanja E. Mehlstäubler^{1,2}

¹Physikalisch-Technische Bundesanstalt, Bundesallee 100, 38116, Braunschweig, Germany.

²Institut für Quantenoptik, Leibniz Universität Hannover, Welfengarten 1, 30167, Hanover, Germany.

*Corresponding author(s). E-mail(s): laura.dreissen@ptb.de;

Gravity is not understood at a quantum mechanical level. In an attempt to formulate a single quantum-consistent theory of the four known fundamental forces, it is suggested that spontaneous breaking of Lorentz symmetry might occur at the Planck scale^{1,2}. In the low-energy limit, such a Lorentz violation would give rise to small shifts of energy levels with non-spherical atomic orbitals³. These could be observed with precision spectroscopy of atoms in a Michelson-Morley type experiment using Earth's rotation⁴⁻⁶. In this work we perform such an experiment in the long-lived electronic $^2F_{7/2}$ manifold of the Yb^+ ion. We exploit the high intrinsic susceptibility of this state to Lorentz violation⁷ and apply an elaborate radio-frequency spin-echoed Ramsey sequence⁸ to investigate the isotropy of space-time with a single trapped ion. A robust composite pulse sequence allows us to extend the coherence time to more than 1 s and accurately compare the orthogonally oriented sub-levels of the Zeeman manifold. With a three times higher sensitivity to Lorentz violation compared to the best test to date⁶, we improve the constraints on all the measured Lorentz symmetry breaking coefficients and set their bounds at the 10^{-21} level. These results represent the most stringent test of this type of Lorentz violation in the electron-photon sector. The method is readily extendable to multiple ions in Coulomb crystals, enabling improved tests of Lorentz symmetry in the near future.

The standard model (SM) of particle physics describes non-gravitational interactions between all particles and fields, while gravitation is described by general relativity in a classical manner. Together, they have explained many physical phenomena observed in the universe remarkably well, but an accurate description of gravity at the quantum level

is lacking. A number of theories that attempt to unify the SM and gravitation at the Planck scale suggest that spontaneous breaking of Lorentz symmetry might occur^{1,9–11}. Lorentz symmetry states that the outcome of a local experiment does not depend on the orientation or the velocity of the apparatus¹². A suppressed effect emerging from Lorentz violation (LV) at the Planck scale could be observed with low-energy experiments in the laboratory. Accurate spectroscopic measurements in trapped particles have reached fractional uncertainties beyond the natural suppression factor¹³, which makes a hypothetical LV measurable in such systems. Furthermore, at high energies, LV could be suppressed by super-symmetry¹⁴. Therefore, accurate low-energy measurements in atoms are suitable to search for LV and complement existing bounds set at high energies with, e.g., particle colliders and astrophysical observations^{15–17}.

Laboratory tests of Lorentz symmetry are based on a similar principle as introduced by Michelson and Morley, who used a rotating interferometer to measure the isotropy of the speed of light¹⁸. Improved bounds on LV for photons have been realized by a variety of experiments involving high-finesse optical and microwave cavities, see e.g. refs. 12, 19–22. Spectroscopic bounds for protons and neutrons were set first using nuclear magnetic resonance on bare nuclei and later with co-magnetometers^{23–25}. More recently, the bounds on LV in the combined electron-photon sector have been explored using precision spectroscopy in trapped ions^{4–6}. These experiments compare energy levels with differently oriented, relativistic, non-spherical electron orbitals as the Earth rotates. Strong bounds on LV were set with trapped $^{40}\text{Ca}^+$ ions, where a decoherence-free entangled state of two ions in the electronic $^2D_{5/2}$ manifold was created to suppress ambient noise^{4,5}. The relatively short 1.2 s radiative lifetime of the $^2D_{5/2}$ state in Ca^+ and the requirement for high fidelity quantum gates limit the scalability and, ultimately, the sensitivity of LV tests with this scheme⁵. The highly relativistic $^2F_{7/2}$ state in the Yb^+ ion is an order of magnitude more sensitive to LV than the $^2D_{5/2}$ state in Ca^+ ^{7,8} and its radiative lifetime was measured to be about 1.6 years²⁶. These beneficial properties were recently exploited in a 45-day comparison of two separate state-of-the-art single-ion optical $^{171}\text{Yb}^+$ clocks, both with a systematic uncertainty at the 10^{-18} level, resulting in a more than ten-fold improvement of the LV bounds⁶.

In this work we present new bounds on LV in the electron-photon sector using a simple, robust and scalable measurement scheme in a single trapped ion experiment. We combine the high susceptibility of the $^2F_{7/2}$ state to LV with an improved radio-frequency (rf) spin-echoed Ramsey sequence^{8,27} to make a direct energy comparison between the nearly orthogonal atomic orbitals of the F -state Zeeman manifold within a single trapped $^{172}\text{Yb}^+$ ion. In this manner, we fully exploit the most sensitive stretched $m = \pm 7/2$ states⁸ and eliminate the requirement of optical clock operation or high-fidelity quantum gates. With the applied composite rf pulse sequence, the influence of fluctuations in the ambient magnetic field on the coherence time is suppressed during the Ramsey measurement, extending the interrogation time $T_D > 1$ s. As a result, the sensitivity of the demonstrated method to LV, which scales as $\sigma_{\text{LV}} \propto \sqrt{1/T_D N_{\text{ion}}}$, is unprecedented already for a single ion ($N_{\text{ion}} = 1$). The rf sequence is robust against both temporal and spatial field inhomogeneities and can be readily applied to a string of N_{ion} trapped ions to further increase the sensitivity to LV in the near future.

The constraints on LV extracted in this work are quantified in the theoretical framework of the standard model extension (SME)²⁸. The SME is an effective field theory in which the SM Lagrangian is extended with all possible terms that are not Lorentz invariant. It is a platform in which LV of all SM particles are described, enabling comparisons between experimental results from many different fields²⁹. In spectroscopic experiments,

a violation of Lorentz symmetry can be interpreted as LV of electrons or photons, because there is no preferred reference system. In this work, we interpret the results as a difference in isotropy between photons and electrons, similar as in refs. 4, 6.

LV in the combined electron-photon sector is quantified by adding a symmetry-breaking tensor $c'_{\mu\nu} = c_{\mu\nu} + k_{\mu\nu}/2$ to the SM Lagrangian^{7,28}, where $c_{\mu\nu}$ and $k_{\mu\nu}$ describe LV for electrons and photons, respectively. For simplicity, the prime is omitted throughout the rest of this work and the extracted coefficients are those of the combined $c'_{\mu\nu}$ tensor, which is taken as traceless and symmetric. The components of the $c_{\mu\nu}$ tensor are frame dependent. A unique definition of the symmetry breaking tensor c_{MN} exists in the Sun-centered, celestial, equatorial frame (SCCEF), illustrated in Fig. 1. In order to make comparisons with other experiments, the $c_{\mu\nu}$ tensor defined in our local laboratory frame is transformed to the SCCEF to constrain the components of the c_{MN} tensor. The full derivation of the transformation can be found in the Methods section.

In a bound electronic systems, LV leads to a small energy shift^{7,8}

$$\delta\mathcal{H} = -\frac{1}{6m_e}C_0^{(2)}T_0^{(2)}, \quad (1)$$

where m_e is the electron mass, the $T_0^{(2)} = \mathbf{p}^2 - 3p_z^2$ operator depends on the direction of the electron's momentum and $C_0^{(2)}$ contains elements of the c_{MN} tensor. For a state with total angular momentum J and projection m onto the quantization axis \hat{z} , the matrix element of the $T_0^{(2)}$ operator is given by⁸

$$\langle J, m | T_0^{(2)} | J, m \rangle = \frac{-J(J+1) + 3m^2}{\sqrt{(2J+3)(J+1)(2J+1)J(2J-1)}} \times \langle J || T^{(2)} || J \rangle. \quad (2)$$

Equations (1) and (2) show that in the SCCEF, LV manifests itself as an energy shift that modulates with Earth's rotation. The magnitude of this shift is dependent on both m^2 and the reduced matrix element $\langle J || T^{(2)} || J \rangle$. The value of the latter is particularly high for the $^2F_{7/2}$ manifold in the Yb^+ ion^{7,8}. The goal of this experiment is to test LV in a single trapped $^{172}\text{Yb}^+$ ion by measuring the energy difference between m -substates in the $^2F_{7/2}$ manifold as the Earth rotates.

The experiment is performed with a single ion, stored in a linear rf Paul-trap, see Fig. 1 b. It is cooled to the Doppler limit of around 0.5 mK on the dipole allowed transition near a wavelength of 370 nm, assisted by a repumper near 935 nm. A set of coils is used to define the quantization axis of $B = 221 \mu\text{T}$, which lies in the horizontal plane with respect to Earth's surface points 20° south of east, see Fig. 1 a. Active feedback is applied on auxiliary coils in three dimensions to stabilize the magnetic field. The $^2F_{7/2}$ state can be efficiently populated via coherent excitation of the highly-forbidden electric octupole (E3) transition (Fig. 1 c) using an ultra-stable frequency-doubled laser at 934 nm³⁰, which is either stabilized only to a cryogenic silicon cavity via a frequency comb³¹ or, optionally, to the single-ion optical $^{171}\text{Yb}^+$ clock³². A Rabi frequency of $\Omega_{\text{E3}}/2\pi = 10 \text{ Hz}$ is achieved on the E3 transition. More details on the experimental apparatus can be found in the Methods section.

The free evolution of a substate $|^2F_{7/2}, m\rangle$ interacting with a magnetic field $\mathbf{B} \equiv B_z \hat{z}$, is given by the Hamiltonian $\mathcal{H}_{\text{free}} = \mathcal{H}_{\text{lin}} + \mathcal{H}_{\text{quad}} = \mu B_z J_z + \kappa J_z^2$, where μ is the magnetic moment. The quadratic term in the Hamiltonian gives rise to an energy shift according to $E_m/h \equiv \kappa/2\pi \times m^2$. The value of $\kappa = \kappa_q + \kappa_{\text{LV}}$ is dependent on the quadrupole shift for the trapped ion in the $^2F_{7/2}$ state and a possible shift due to LV, respectively. The

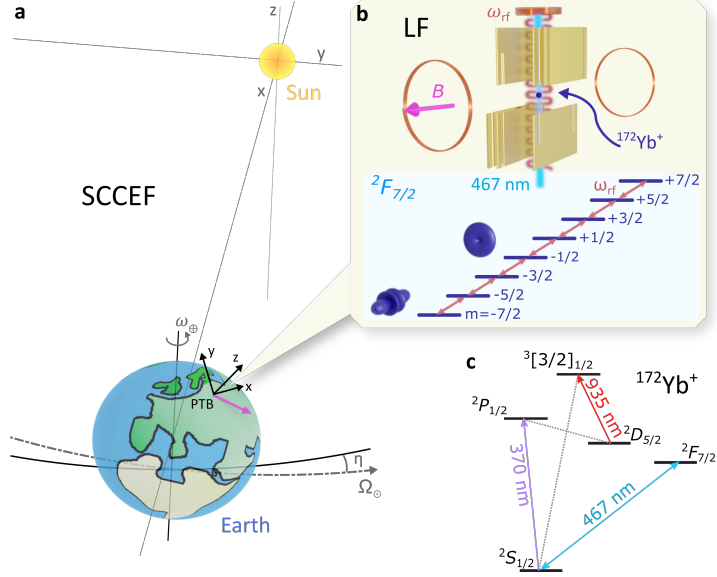


Fig. 1 A schematic overview of the experimental principle. **a** In the laboratory frame (LF) coordinate system z points vertically upwards, y points North and x points east. The fixed quantization axis \mathbf{B} (pink arrow) in the LF coordinate system lies in the horizontal plane and points 20° south of x and probes different directions in the SCCEF as the Earth rotates around its axis (ω_\oplus) and orbits the Sun (Ω_\odot). **b** In the LF a single $^{172}\text{Yb}^+$ ion is trapped in a segmented rf trap. Two coils generate a quantization field of $B = 221 \mu\text{T}$. The electron orbitals of the $m = \pm 1/2$ and $m = \pm 7/2$ Zeeman sublevels in the $^2F_{7/2}$ state orient themselves orthogonally to each other. The $^2F_{7/2}$ state is population via the E3 transition near 467 nm. The m substates are coupled via the rf magnetic field at ω_{rf} created with a coil that is placed 5.5 cm above the ion. **c** A simplified energy level diagram of $^{172}\text{Yb}^+$, showing the optical E3 transition and the transitions near 370 nm and 935 nm used for Doppler cooling and state detection.

contribution of LV to κ is given by⁸

$$\frac{\kappa_{\text{LV}}}{2\pi} = 5.1 \times 10^{15} \text{ Hz} \times C_0^{(2)}, \quad (3)$$

where $C_0^{(2)}$ contains components of the c_{MN} tensor in the SCCEF, see Methods. A modulation of the quadratic contribution to the Zeeman splitting in the $^2F_{7/2}$ manifold is measured with rf Ramsey spectroscopy. The m -levels are coupled via a rf magnetic field supplied to the ion by a resonant LC circuit. The coupling term in the Hamiltonian is given by $\mathcal{H}_{\text{coupling}} = \Omega_F \cos(\omega_{\text{rf}}t + \phi) J_x$, where $\Omega_F/2\pi = 33 \text{ kHz}$ is the multilevel Rabi frequency and ω_{rf} and ϕ are the frequency and the phase of the rf field, respectively. The rf frequency is close to resonance with the, to first order, equidistant m -levels given by $\omega_{\text{rf}}/2\pi = \mu B_z/h + \delta(t)/2\pi \approx 3.5 \text{ MHz}$, where $\delta(t)$ is a small detuning from temporal drifts in the ambient magnetic field. The full Hamiltonian of the system in the interaction picture after applying the rotating wave approximation is given by

$$\mathcal{H} = \delta(t) J_z + \kappa J_z^2 + \Omega_F [J_x \cos(\phi) - J_y \sin(\phi)], \quad (4)$$

where the changes in $\delta(t)$ and κ should be much slower than the π -pulse time of $t_\pi = \pi/\Omega_F = 15 \mu\text{s}$.

A composite rf pulse sequence, based on a spin-echoed Ramsey scheme, is implemented to mitigate the influence of $\delta(t)$, while retaining a high sensitivity to variations of κ . A

schematic overview of the rf sequence is shown in Fig. 2 a. Starting from either one of the $m = \pm 1/2$ states, a $\pi/2$ -pulse, i.e. $t_{\pi/2} = t_{\pi}/2$, with phase $\phi = 0$ spreads the population over all the Zeeman sublevels. A modulation sequence, consisting of ten repetitions of the form $[t_w] - [t_{\pi}(\phi_i)] - [t_w]$, is applied to cancel dephasing from $\delta(t)$. Here t_w is the time in which the state freely evolves and $t_{\pi}(\phi_i)$ indicates a π -pulse with phase ϕ_i . In our experimental environment, dephasing is successfully canceled for $t_w = 100 \mu\text{s}$. The phases ϕ_i of the consecutive π -pulses are set to $(0, 4, 2, 4, 0, 0, 4, 2, 4, 0) \pi/5$, for which the modulation sequence is shown to be highly robust against pulse errors from, e.g., detuning and intensity variations²⁷. At the end of the sequence, a $\pi/2$ -pulse with phase $\phi = \pi$ retrieves a fraction P_f of the population back into the initial $m = \pm 1/2$ state. The Ramsey dark-time, i.e. the time in which the state freely evolves, can be extended to $T_D = N \times 20 t_w$ by repeating the modulation sequence N times.

The retrieved fraction P_f is dependent on the phase κT_D acquired during the free-evolution time, which stems from the quadratic term in the Hamiltonian of equation (4). Therefore, κ_{LV} can be extracted from a measurement of P_f at a fixed T_D . Since a hypothetical LV would manifest itself as a modulation of κ at frequencies related to a sidereal day ($\omega_{\oplus}/2\pi = 1/23.934 \text{ h}$), a signal of LV is characterized by oscillations of P_f at the same modulation frequencies. A measurement of P_f is realized by de-exciting the ion via the E3 transition to the $^2S_{1/2}$ state, where it can be detected by collecting fluorescence on the dipole allowed $^2S_{1/2} \rightarrow ^2P_{1/2}$ transition.

The highest measurement accuracy is achieved when the measured quantity P_f is most sensitive to variations of κ , i.e. $|dP_f/d\kappa|$ is maximized, which is the case at $\kappa T_D = 0.15 \text{ rad}$ ⁸. Using the axial secular frequency of $266(5) \text{ kHz}$ set during the measurement campaign and the quadrupole moment of the $^2F_{7/2}$ state³³, κ_q was calculated to be $0.13(3) \text{ rad/s}$, see the Methods section. The corresponding optimal Ramsey dark time is $T_D = 1.15 \text{ s}$.

A schematic overview of the full experimental sequence is shown in Fig. 2 b. Stable long-term operation of the experiment is required to resolve oscillation periods related to a potential LV, i.e. 11.967 and 23.934 hours. Especially the center frequency of the E3 transition is sensitive to external perturbations from, e.g., magnetic field drifts and intensity fluctuations. Therefore, a 4-point servo-sequence of two opposite Zeeman transitions $|^2S_{1/2}, m = \pm 1/2\rangle \rightarrow |^2F_{7/2}, m = \pm 1/2\rangle$ at half the linewidth is applied every $n = 50$ measurement runs to follow the E3 center frequency. For details on this technique, see e.g. ref. 34. On average a population transfer of 80 % is realized to the $^2F_{7/2}$ state via the E3 transition using the servo-sequence.

After the E3 servo and 2.5 s of compilation time for the rf pulse sequence, a measurement starts with a detection pulse to determine if the ion is cooled and prepared in the correct initial $|^2S_{1/2}, m = \pm 1/2\rangle$ state. If this is not the case, consecutive repumping and recooling sequences are applied. To save overhead time, either the $|^2F_{7/2}, m = +1/2\rangle$ or the $|^2F_{7/2}, m = -1/2\rangle$ state is populated via E3 excitation of the same Zeeman transition as was addressed last by the servo sequence. Another detection pulse is applied to determine if the E3 excitation was successful. A single rf modulation sequence of $T_m = 10 \times t_{\pi} + 20 \times t_w = 2.15 \text{ ms}$ is repeated $N = 575$ times to reach $T_D = 1.15 \text{ s}$. The full rf sequence runs for $T_{\text{rf}} = N \times T_m + 2 \times t_{\pi/2} = 1236.27 \text{ ms}$. A third detection pulse is applied to determine if the ion was quenched to the ground state during the rf sequence due to, e.g., a collision with background gas. The ion is de-excited on the E3 transition and, with a final detection pulse, P_f is measured. At the end of the measurement sequence, the ion is re-cooled and prepared in the required $|^2S_{1/2}, m = \pm 1/2\rangle$ electronic ground state for the next measurement run. Data points are only considered

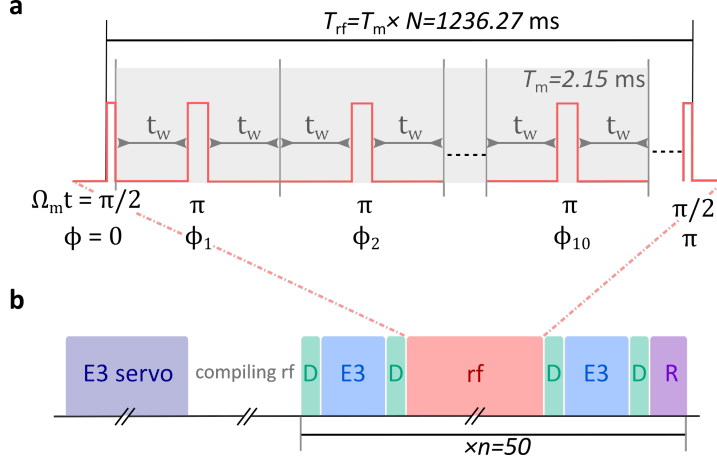


Fig. 2 Pulse sequences. **a** The applied composite rf pulse sequence is a more robust version of a spin-echoed Ramsey scheme. A Ramsey sequence of $T_{\text{rf}} = 1236.27$ ms starts and ends with a $\pi/2$ -pulse. A 2.15 ms-long modulation sequence of 10 π -pulses with phases ϕ_i ($i = 1 \dots 10$) each spaced by $2t_w = 200 \mu\text{s}$ is repeated $N = 575$ times to cancel dephasing due to ambient magnetic field noise. The phases ϕ_i are chosen such (see text) that the sequence is robust against pulse errors. **b** Every $n = 50$ measurements, a 4-point servo sequence (E3 servo) of 40 s is applied to follow the E3 center frequency, after which the rf sequence is compiled for 2.5 s. The measurement sequence consists of two 50 ms-long E3 pulses (E3), the rf pulse sequence (rf) of 1236.27 ms, and four detection pulses (D) of 2.5 ms and a sequence at the end of 20 ms for state preparation (R) for the next measurement run. During post-selection, the data points are considered valid if the ion was in the desired state during the first three detection pulses.

valid when the ion was in the correct state at both the second and the third detection stage. After post-selection of valid data points an average contrast of 0.77(6) is reached. Including additional overhead from compilation time, data points are obtained at a rate of $1/191 \text{ s}^{-1}$.

The data acquired over a period of 912 h, with an up-time of 591 h, is shown in Fig. 3 a. Data points are averaged in equidistant bins of 15 min. The measured population is decomposed in two parts $P_f = P(\kappa_q) + P(\kappa_{\text{LV}})$, where $P(\kappa_q)$ gives rise to a constant offset of $P_0 = 0.39$ and $P(\kappa_{\text{LV}}) = dP_f/d\kappa \times \kappa_{\text{LV}}$ contains a potential LV signal. To extract κ_{LV} from P_f , a high-pass filter is applied with a cutoff frequency of $\nu_c = 5 \mu\text{Hz}$, removing P_0 and slow variations ($\tau_{\text{drift}} < 2.5$ days) caused by drifts in the E3 excitation probability and the slope $dP_f/d\kappa|_{\kappa=0.13(3)} = -4.4(4)$ is calculated. More details on the data handling and the measurement sensitivity can be found in the Methods section.

In search of LV at Fourier frequencies of ω_{\oplus} and $2\omega_{\oplus}$, the data is fitted globally to the fit function

$$\begin{aligned} \kappa_{\text{LV}} = & 2\pi \times 5.1 \times 10^{15} \times [-3 \sin(2\chi) c_{XZ} \cos(\omega_{\oplus} T) - 3 \sin(2\chi) c_{YZ} \sin(\omega_{\oplus} T) \\ & - \frac{3}{2} c_{X-Y} \sin^2(\chi) \cos(2\omega_{\oplus} T) - 3 c_{XY} \sin^2(\chi) \sin(2\omega_{\oplus} T)], \end{aligned} \quad (5)$$

from which the individual components of the c_{MN} tensor in the SCCEF are extracted, where $c_{X-Y} = c_{XX} - c_{YY}$. The fit overlays the data in Fig. 3 a and the residuals from the fit are shown in Fig. 3 b, from which the reduced chi-square of $\chi^2 = 0.92$ is extracted. The fitted values of the components of the c_{MN} tensor are given in Tab. 1. For comparison, the values obtained by refs. 5, 6 are also presented. The uncorrelated linear combination of the fit parameters, calculated by diagonalizing the covariance matrix, are given in the lower part of Tab. 1. The spectral content of the data, shown in Fig. 3 c, is analyzed

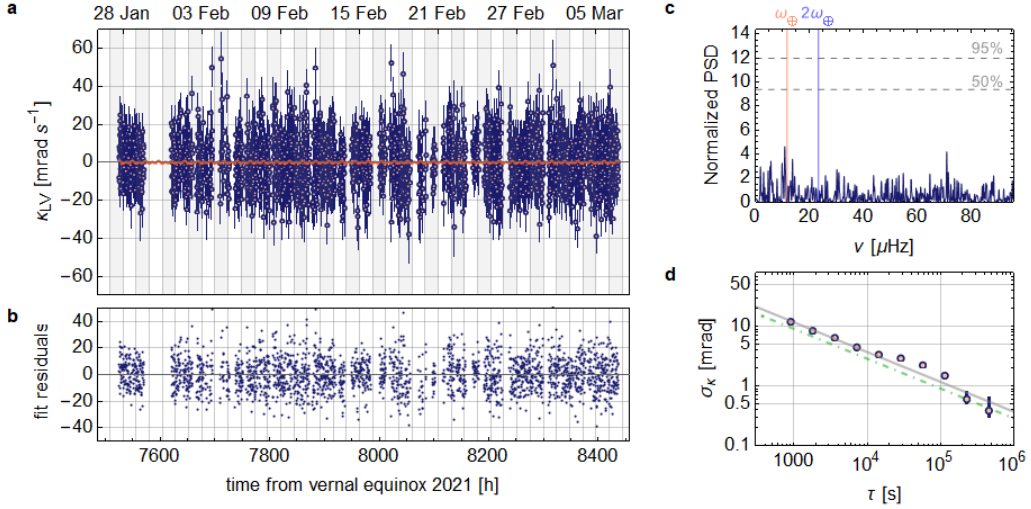


Fig. 3 Data acquired over a period of 912 h with an up-time of 591 h. **a** The measured value of κ_{LV} (blue data points) extracted from $P_{\hat{f}}$. The error bars correspond to the 1σ uncertainty. Data points are binned at 15 minute intervals. The data is fitted to equation (5) (red line) from which bounds are set on components of the c_{MN} tensor. **b** The residuals of the fit with a reduced $\chi^2 = 0.92$. **c** A Lomb-Scargl periodogram for spectral analysis of irregularly spaced data. The vertical lines indicate the sidereal day frequency ω_{\oplus} (red) and its second harmonic $2\omega_{\oplus}$ (blue). The dashed lines indicate the statistical significance level, i.e. p-value, of the peaks³⁵. **d** The Allan deviation of the data points and the corresponding fit (gray line) $\sigma_{\kappa} = 372(9) \text{ mrad } \tau^{-1/2}$. The expected stability from quantum projection noise (dashed-dotted green line) is 29(3) % lower.

using a Lomb-Scargl periodogram³⁵, which is specifically suited for spectral analysis of irregularly spaced data. The statistical significance level, i.e. p-values³⁵, of 50 % and 95 % are indicated by horizontal lines.

The fit results show that the extracted values for c_{X-Y} , c_{XZ} and c_{YZ} are consistent with zero within a 1σ uncertainty. Only c_{XY} shows a 1.1σ deviation from zero, but spectral analysis does not show a significant Fourier component at $2\omega_{\oplus}$. Therefore, we conclude that we do not find evidence of LV, in agreement with previous work^{5,6}. The stability of the data points is analyzed by calculating the Allan deviation, as shown in Fig. 3d. The data averages down as $\sigma_{\kappa} = 372(9) \text{ mrad } \tau^{-1/2}$, which is 29(3) % higher than what is expected from quantum projection noise.

The presented results set the most stringent bounds on this type of LV in the combined electron-photon sector. The uncertainties on all the extracted coefficients of the c_{MN} tensor are at the 10^{-21} level. Due to the experimental geometry, see Methods, a higher sensitivity is reached for signals that oscillate at $2\omega_{\oplus}$ than those that oscillate at ω_{\oplus} . The bounds on c_{X-Y} are improved by a factor of 2.2 in 1.8 times less total averaging time, demonstrating a 3-times higher sensitivity to LV compared to the previous most sensitive measurement⁶. The tightest constraint of 3.9×10^{-21} is achieved on c_{XY} . In this work, coefficients of the first and second harmonic order of the sidereal day modulation frequency were considered. However, due to the high total angular momentum of the $^2F_{7/2}$ state, the applied method is sensitive to LV at harmonics of up to sixth order^{36,37}. Therefore, in combination with new many-body calculations, experimental constraints can be translated into bounds on a larger number of coefficients in the future³⁷. The demonstrated method is technically less demanding and more robust than alternative methods requiring optical clock operation or high-fidelity entanglement gates^{5,6}. It

correlated LV parameters	this work	$^{171}\text{Yb}^+$ limits ⁶	$^{40}\text{Ca}^+$ limits ⁵
c_{X-Y}	$(-5.2 \pm 7.8) \times 10^{-21}$	$(-0.5 \pm 1.7) \times 10^{-20}$	$(6.2 \pm 9.2) \times 10^{-19}$
c_{XY}	$(4.4 \pm 3.9) \times 10^{-21}$	$(-7.0 \pm 8.1) \times 10^{-21}$	$(2.4 \pm 4.8) \times 10^{-19}$
c_{XZ}	$(-5.0 \pm 9.3) \times 10^{-21}$	$(0.8 \pm 1.3) \times 10^{-20}$	$(0.8 \pm 2.1) \times 10^{-19}$
c_{YZ}	$(6.3 \pm 8.9) \times 10^{-21}$	$(1.0 \pm 1.3) \times 10^{-20}$	$(-3.1 \pm 2.2) \times 10^{-19}$
uncorrelated linear combinations of parameters			this work
$0.70c_{XZ} + 0.26c_{YZ} + 0.51c_{X-Y} + 0.42c_{XY}$			$(0.0 \pm 1.0) \times 10^{-20}$
$0.24c_{XZ} - 0.61c_{YZ} + 0.46c_{X-Y} - 0.59c_{XY}$			$(-13.8 \pm 9.6) \times 10^{-21}$
$-0.47c_{XZ} - 0.50c_{YZ} + 0.38c_{X-Y} + 0.62c_{XY}$			$(3.0 \pm 7.2) \times 10^{-21}$
$-0.48c_{XZ} + 0.56c_{YZ} + 0.61c_{X-Y} - 0.29c_{XY}$			$(-0.4 \pm 3.5) \times 10^{-21}$

Table 1 The extracted correlated components of the c_{MN} tensor compared to existing limits from refs.⁶ and⁵. All uncertainties represent a 1σ interval. The uncorrelated linear combination of parameters is obtained by diagonalizing the covariance matrix.

is readily scalable to multiple N_{ions} in linear ion Coulomb crystals to further enhance the sensitivity by a factor $\sqrt{N_{\text{ion}}}$. The implemented composite rf pulse sequence is highly robust against errors originating from spatial and temporal fluctuations in both the ambient field and the rf field. Therefore, the coherence time is not expected to significantly decrease for larger ion numbers, in contrast to measurement schemes that rely on entangled states⁵. For efficient population transfer via the E3 transition, advanced cooling techniques, such as EIT³⁸ or Sisyphus cooling^{39,40}, might be advantageous in larger ion crystals. The long lifetime of the $^2F_{7/2}$ state in Yb^+ ²⁶ does not significantly limit the coherence time and with several technical improvements, longer interrogation times might be reached. Therefore, the boundaries of Lorentz symmetry tests can be pushed to the 10^{-22} level with a string of 10 ions in the near future with the presented method.

Methods

Experimental details

A single $^{172}\text{Yb}^+$ ion is trapped in a segmented rf Paul-trap^{41,42}. The radial confinement is set with an rf electric field supplied by a resonant circuit at a frequency of $\Omega_{\text{rf}}/2\pi = 24.38$ MHz, while the axial confinement is set by dc voltages supplied to the trapping segment and the neighboring segments. With the applied confinement, the secular frequencies are $\omega(\text{rad1}, \text{rad2}, \text{ax})/2\pi = (775, 510, 266)$ kHz. Micromotion is measured on a daily basis with the photon correlation technique⁴³ and compensated in three dimensions to typically $E_{\text{rf}} < 100$ V/m. The quantization field of $B = 221$ μT lies in the horizontal plane under an angle of 25° to the trap axis. The B -field is measured with a sensor near the vacuum chamber and active feedback is applied in three dimensions via current modulation of six auxiliary coils.

The ion is cooled to approximately 0.5 mK, close to the Doppler limit, on the dipole allowed $^2S_{1/2} \rightarrow ^2P_{1/2}$ transition assisted by a repumper laser near 935 nm. Fluorescence from the decay of the $^2P_{1/2}$ state is collected by a lens of $N/A = 0.27$ and imaged onto the electron-multiplying charge-coupled device (EMCCD) camera⁴⁴. This enables state detection via the electron shelving technique. The ion can be prepared in either the $|^2S_{1/2}, m = -1/2\rangle$ or the $|^2S_{1/2}, m = +1/2\rangle$ state using circular polarized beam near 370 nm pointing along the direction of the quantization axis. The 467 nm laser for excitation on the E3 transition lies in the radial plane and its beam waist is $26(3) \times 38(3)$ μm at the ion. The power is stabilized to 6.0(2) mW, at which a Rabi frequency of $\Omega_{\text{E3}}/2\pi = 10$ Hz is reached. The light is frequency-shifted and pulsed using acousto-optic modulators.

The resonant rf coil, consisting of 27 turns wound at a diameter of 4.5 cm, is placed 5.5 cm above the ion. The resonance frequency of the coil is $\omega_{\text{res}}/2\pi = 3.5147(7)$ MHz and it is driven by a signal derived from a direct digital synthesizer (DDS), referenced to a stable 100 MHz signal from a hydrogen maser. At $B = 221$ μT , the resonance frequency between the m -levels in the $^2F_{7/2}$ state is $\omega_{\text{rf}}/2\pi = 3.52$ MHz, close to the resonance frequency of the coil. The achieved multi-level Rabi frequency is $\Omega_F/2\pi = 33$ kHz. The ambient magnetic field is monitored throughout the measurement campaign via data acquired in the E3 servo sequence. Drifts are observed at the level of $\Delta B = 100$ nT, corresponding to a detuning $\Delta\omega_{\text{rf}}/2\pi = 1.6$ kHz. The frequency supplied to the coils is actively adjusted to remain in resonance with the frequency given by the linear Zeeman splitting. For this purpose, the resonance frequency as a function of magnetic field was calibrated to be $\omega_{\text{rf}}(B)/2\pi = [1.581(1.6)B + 0.0162(3)]$ in MHz. For further details on the experimental set-up, see refs. 30, 41, 44, 45.

Relating the lab frame to the SCCEF

The elements of the $c_{\mu\nu}$ tensors are dependent of the local laboratory frame. In order to compare our results with those from other experiments, we transform the components of the local c_{mn} tensor to the sun-centered, celestial-equatorial frame (SCCEF). We follow a similar derivation as given in ref. 6.

The relation between the components of c_{mn} in the lab frame and c_{MN} in the SCCEF is given by

$$c_{mn} = \Lambda_m^M \Lambda_n^N c_{MN}, \quad (6)$$

where Λ is the Lorentz transformation matrix, which consists of rotations and boosts in the lab frame relative to the SCCEF. Our lab frame has its origin at a colatitude of

$\chi = 37.7^\circ$ and a longitude of $\lambda = 10.5^\circ$ (PTB Braunschweig, Germany). In the local coordinate system, \hat{x} points towards the east, \hat{y} points towards the north and \hat{z} points upward. The rotation matrix that maps the SCCEF coordinate frame to that of the lab is given by

$$\mathbf{R} = \begin{pmatrix} -\sin(\omega_\oplus T) & \cos(\omega_\oplus T) & 0 \\ -\cos(\chi) \cos(\omega_\oplus T) & -\cos(\chi) \sin(\omega_\oplus T) & \sin(\chi) \\ \sin(\chi) \cos(\omega_\oplus T) & \sin(\chi) \sin(\omega_\oplus T) & \cos(\chi) \end{pmatrix}, \quad (7)$$

where $\omega_\oplus/2\pi = 1/23.934$ h is the angular frequency of a sidereal day. Our quantization magnetic field B lies in the xy plane and points 20° south of east. Similar as in ref. 6, we calculate a virtual location on Earth's surface, where B points vertically upward by only changing the origin of the coordinate system, not affecting transformation formulas between the lab frame and the SCCEF frame. This yields $\chi_n = 102.1^\circ$ and $\lambda_n = 84.4^\circ$. Substituting $\chi = \chi_n$ and $\lambda = \lambda_n$ values in equation (7) and setting $T = 0$ at the moment the z axis of the new location points towards the Sun on the day of the Vernal equinox, in this case 03:59:24 UTC, March 20, 2021 yields the proper transformation equations. The boost of the experimental frame as seen from the SCCEF is given by

$$\boldsymbol{\beta} = \begin{pmatrix} \beta \sin(\Omega_\odot T) \\ -\beta \cos(\eta) \cos(\Omega_\odot T) \\ -\beta \sin(\eta) \cos(\Omega_\odot T) \end{pmatrix}, \quad (8)$$

where $\Omega_\odot/2\pi = 1/(365.256 \times 24\text{h})$ is the angular frequency of a sidereal year, $\beta = 1 \times 10^{-4}$ is the magnitude of the boost from the orbital velocity and $\eta = 23.4^\circ$ is the angle between the ecliptic plane and the Earth's equatorial plane. Here the boost from the Earth's rotation has been neglected as it is two orders of magnitude smaller ($\beta_L = 1.5 \times 10^{-6}$). Using the rotations and boosts, the Lorentz transformation that maps $c_{\mu\nu}$ from the SCCEF to the lab frame is given by

$$\Lambda = \begin{pmatrix} 1 & -\beta^1 & -\beta^2 & -\beta^3 \\ -(R \cdot \beta)^1 & R^{11} & R^{12} & R^{13} \\ -(R \cdot \beta)^2 & R^{21} & R^{22} & R^{23} \\ -(R \cdot \beta)^3 & R^{31} & R^{32} & R^{33} \end{pmatrix}, \quad (9)$$

Using equation (9), the parameter $C_0^{(2)}$ can now be expressed in terms of components of c_{MN} in the SCCEF using the Lorentz transformation. It is given by

$$C_0^{(2)} = A_0 + \sum_j [C_j \cos(\omega_j T) + S_j \sin(\omega_j T)], \quad (10)$$

where A_0 is a constant offset, ω_j contains all linear combinations of ω_\oplus and Ω_\odot , and C_j and S_j are the respective amplitudes as given in Tab. S1.

With the high-pass filter applied to the data, we are sensitive only to signals that oscillate at frequencies larger than $\nu_c = 5 \mu\text{Hz}$. Therefore the Lorentz violating signal is given by

$$\begin{aligned} C_0^{(2)} = & -3 \sin(2\chi) c_{XZ} \cos(\omega_\oplus T) - 3 \sin(2\chi) c_{YZ} \sin(\omega_\oplus T) \\ & - \frac{3}{2} (c_{XX} - c_{YY}) \sin^2(\chi) \cos(2\omega_\oplus T) - 3 c_{XY} \sin^2(\chi) \sin(2\omega_\oplus T). \end{aligned} \quad (11)$$

ω_j	C_j	S_j
ω_\oplus	$-3\sin(2\chi)c_{xz} + 2c_{TY}\beta_L$	$-3\sin(2\chi)c_{YZ} - 2c_{TX}\beta_L$
$2\omega_\oplus$	$-\frac{3}{2}(c_{XX} - c_{YY})\sin^2(\chi)$	$-3c_{XY}\sin^2(\chi)$
Ω_\odot	$-\frac{1}{2}\beta(3\cos(2\chi) + 1)(c_{TY}\cos(\eta) - 2c_{TZ}\sin(\eta))$	$\frac{1}{2}\beta c_{TX}(3\cos(2\chi) + 1)$
$2\Omega_\odot$	0	0
$\Omega_\odot - \omega_\oplus$	$\frac{3}{2}\beta c_{TX}\sin(\eta)\sin(2\chi)$	$-\frac{3}{2}\beta\sin(2\chi)[c_{TY}\sin(\eta) + c_{TZ}(1 + \cos(\eta))]$
$\Omega_\odot + \omega_\oplus$	$\frac{3}{2}\beta c_{TX}\sin(\eta)\sin(2\chi)$	$-\frac{3}{2}\beta\sin(2\chi)[c_{TZ}(1 - \cos(\eta)) - c_{TY}\sin(\eta)]$
$2\Omega_\odot - \omega_\oplus$	0	0
$2\Omega_\odot + \omega_\oplus$	0	0
$\Omega_\odot - 2\omega_\oplus$	$-3\beta c_{TY}\cos^2(\eta/2)\sin^2(\chi)$	$-3\beta c_{TX}\cos^2(\eta/2)\sin^2(\chi)$
$\Omega_\odot + 2\omega_\oplus$	$3\beta c_{TY}\sin^2(\eta/2)\sin^2(\chi)$	$-3\beta c_{TX}\sin^2(\eta/2)\sin^2(\chi)$
$2\Omega_\odot - 2\omega_\oplus$	0	0
$2\Omega_\odot + 2\omega_\oplus$	0	0

Table S1 The angular frequencies and the corresponding amplitudes contributing to $C_0^{(2)}$ in the SCCEF as a function of the colatitude χ and the angle between the ecliptic plane and the Earth's equatorial plane η .

Combining equation (11) with the sensitivity of κ_{LV} to $C_0^{(2)}$ ⁸ yields

$$\begin{aligned} \kappa_{LV} = 2\pi \times 5.1 \times 10^{15} \times & [-3 \sin(2\chi) c_{XZ} \cos(\omega_{\oplus} T) - 3 \sin(2\chi) c_{YZ} \sin(\omega_{\oplus} T) \\ & - \frac{3}{2} (c_{XX} - c_{YY}) \sin^2(\chi) \cos(2\omega_{\oplus} T) - 3 c_{XY} \sin^2(\chi) \sin(2\omega_{\oplus} T)]. \end{aligned} \quad (12)$$

The stability of κ_{LV} was measured to be $\sigma_{\kappa} = 372(9) \text{ mrad } \tau^{-1/2}$, from which we can extract the stability of $C_0^{(2)}$ to be $\sigma_{C_0^{(2)}} = 1.16 \times 10^{-17} \tau^{-1/2}$.

The measurement sensitivity

The quadratic term in the free Hamiltonian for state $|J, m\rangle$ interacting with a magnetic field $\mathbf{B} = B_z \hat{z}$ is given by $\mathcal{H}_{\text{quad}} = \kappa J_z^2$. It scales with $\kappa = \kappa_q + \kappa_{LV}$, where the first term is given by the quadrupole shift and the second term is given by a potential LV. The quadrupole shift can be calculated using⁴⁶

$$\Delta\nu_{\text{quad}} = \frac{1}{4} \frac{J(J+1) - 3m^2}{J(2J-1)} \frac{1}{h} \Theta(^2F_{7/2}) \frac{dE}{dz} [3 \cos^2(\beta) - 1], \quad (13)$$

The quadrupole moment of the $^2F_{7/2}$ state is given by $\Theta(^2F_{7/2}) = -0.0297(5) e a_0^2$ ³³, where e is the electron charge and a_0 is the Bohr radius. The electric field gradient is given by $dE/dz = -m_{\text{ion}} \omega_z^2 / q$ for a single trapped ion with mass m_{ion} and charge q at the equilibrium position of the trap. The angle between the quantization axis and the

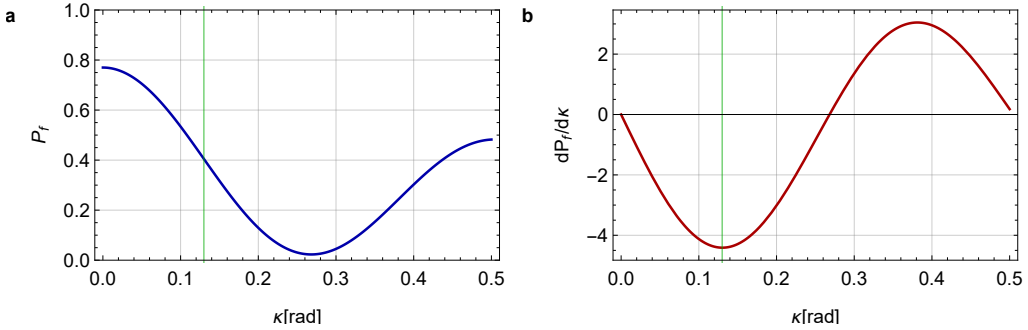


Fig. S1 The sensitivity of the measured quantity P_f to variations in κ . **a** The calculated final population P_f as a function of κ at $T = 1.15$ s, where the experimentally achieved contrast of $0.77(6)$ was taken into account. **b** The derivative $dP_f/d\kappa$ as a function of κ at $T = 1.15$ s. The measurement sensitivity at $\kappa_q = 0.13$ (green vertical line in **a** and **b**) is given by $dP_f/d\kappa|_{\kappa=0.13} = -4.4$.

principle axis of the trap is in our case $\beta = 25^\circ$. The corresponding value for κ_q is given by

$$\frac{\kappa_q}{2\pi} = -\frac{3}{4J(2J-1)} \frac{1}{h} \Theta(^2F_{7/2}) \frac{dE}{dz} [3 \cos^2(\beta) - 1]. \quad (14)$$

At typical values of the axial secular frequency in our trap $\omega_{\text{ax}}/2\pi = (200 - 290) \text{ kHz}$, the quadrupole shift is $\nu_{\text{quad}} = 60 - 125 \text{ mHz}$, corresponding to $\kappa_q = 0.075 - 0.150 \text{ rad/s}$. The fraction P_f retrieved back into the $m = \pm 1/2$ state at the end of the rf sequence is dependent on the acquired phase κT_D , where T_D is the Ramsey dark time. At $\kappa T_D = 0.15 \text{ rad}$, the slope $|dP_f/d\kappa|$ is maximum and the highest measurement sensitivity is reached.

In the experiment, $\kappa = 0.13(3)$ for which an optimum Ramsey dark-time of $T_D = 1.15$ s is found. Using the average achieved contrast of $(P_{f,\max} - P_{f,\min}) / (P_{f,\max} + P_{f,\min}) = 0.77$, P_f and $dP_f/d\kappa$ are calculated as a function of κ , as shown in Fig. S1 a and b, respectively. At $\kappa_q = 0.13(3)$, the sensitivity of P_f to variations of κ is calculated to be $dP_f/d\kappa|_{\kappa=0.13(3)} = -4.4(4)$. The uncertainty on κ_{LV} stemming from $\Delta(dP_f/d\kappa|_{\kappa=0.13(3)}) = 0.4$ is added to $\Delta\kappa_{LV}$ in quadrature.

Data handling

The E3 servo sequence is based on four measured populations at half the linewidth of the two opposite Zeeman transitions $|^2S_{1/2}, m = \pm 1/2\rangle \rightarrow |^2F_{7/2}, m = \pm 1/2\rangle$. The average value of the four measured data points are equal to $p_{E3}/2$, where p_{E3} is the excitation probability of the E3 transition. Via the E3 servo sequence, repeated every 50 data points, p_{E3} is monitored throughout the measurement campaign.

Slow drifts of p_{E3} are observed on timescales of $\tau < 2.5$ days, corresponding to Fourier frequencies of $\omega/2\pi < 5$ μ Hz, due to changes in, e.g., beam pointing and ambient noise. The quantity P_f is detected via de-excitation from the $^2F_{7/2}$ on the E3 transition and it is, therefore, highly correlated with p_{E3} . To quantify the correlation, data points are averaged over a time span of about one day and Pearson's correlation factor is calculated to be 0.9. The number of measurements per averaged data point are not equal for p_{E3} and P_f and, therefore, the standard deviation of the two data sets are significantly different. For visualization purposes, the measured quantities are scaled by their respective standard deviation and plotted together with the 95% confidence interval, see Fig. S2. Note that Pearson's correlation factor differs from 1, because the p_{E3} and P_f are not measured at exactly the same time, but rather in an alternating fashion.

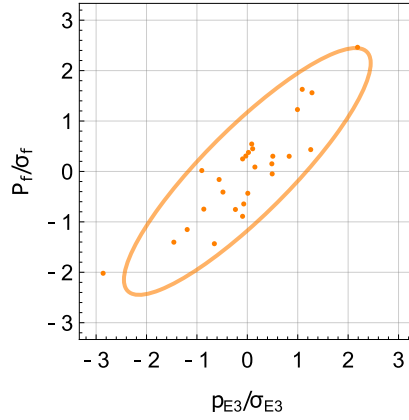


Fig. S2 Correlation between the E3 excitation probability p_{E3} and the measured quantity P_f averaged over a time span of about one day. The data points show p_{E3}/σ_{E3} and P_f/σ_f after subtracting the offset of 22.6 and 9.2, respectively. Pearson's correlation is calculated to be 0.90. The ellipse indicates the 95% confidence interval.

The measured data points P_f are corrected for slow drifts of p_{E3} . Residual slow variations that are not clearly connected to p_{E3} are observed in the data at $\omega/2\pi = 1.65$ μ Hz, related to a fluctuation on the timescale of a week. This Fourier component is removed from the data with a high-pass filter using a Hamming window with a cut-off frequency of $\nu_c = 5$ μ Hz. Bounds on LV at frequencies ω_{\oplus} and $2\omega_{\oplus}$ are extracted from the filtered

data using a fit to equation (5).

To investigate the possible influence from the filter on the result, data points are simulated with Fourier components at $\omega/2\pi = 1.5\mu\text{Hz}$, $\omega = \omega_{\oplus}$ and $\omega = 2\omega_{\oplus}$, mimicking the observed slow drifts and a hypothetical LV signal, respectively. Exactly the same time stamps are used for the simulated data as for the experiment. The high-pass filter is applied to the simulated data with different values of ν_c , after which it is fitted to extract the amplitudes at ω_{\oplus} and $2\omega_{\oplus}$. The retrieved amplitudes do not significantly differ from the simulated amplitudes for cut-off frequencies between $2 < \nu_c < 10\mu\text{Hz}$. To validate this, the actual experimental data is also filtered with different values of ν_c in the range of $2 < \nu_c < 10\mu\text{Hz}$. The extracted amplitudes at ω_{\oplus} and $2\omega_{\oplus}$ from the fit to equation (5) do not show a significant deviation for different values of ν_c in this range.

References

1. Kostelecký, V. A. & Samuel, S. Spontaneous breaking of Lorentz symmetry in string theory. *Phys. Rev. D* **39**, 683–685 (1989). URL <https://link.aps.org/doi/10.1103/PhysRevD.39.683>. <https://doi.org/10.1103/PhysRevD.39.683> .
2. Kostelecký, V. A. Gravity, Lorentz violation, and the standard model. *Phys. Rev. D* **69**, 105009 (2004). URL <https://link.aps.org/doi/10.1103/PhysRevD.69.105009>. <https://doi.org/10.1103/PhysRevD.69.105009> .
3. Kostelecký, V. A. & Lane, C. D. Constraints on Lorentz violation from clock-comparison experiments. *Phys. Rev. D* **60**, 116010 (1999). URL <https://link.aps.org/doi/10.1103/PhysRevD.60.116010>. <https://doi.org/10.1103/PhysRevD.60.116010> .
4. Pruttivarasin, T. *et al.* Michelson–Morley analogue for electrons using trapped ions to test Lorentz symmetry. *Nature* **517** (7536), 592–595 (2015) .
5. Megidish, E., Broz, J., Greene, N. & Häffner, H. Improved test of local Lorentz invariance from a deterministic preparation of entangled states. *Phys. Rev. Lett.* **122**, 123605 (2019). URL <https://link.aps.org/doi/10.1103/PhysRevLett.122.123605>. <https://doi.org/10.1103/PhysRevLett.122.123605> .
6. Sanner, C. *et al.* Optical clock comparison for Lorentz symmetry testing. *Nature* **567** (7747), 204–208 (2019) .
7. Dzuba, V. A. *et al.* Strongly enhanced effects of Lorentz symmetry violation in entangled Yb^+ ions. *Nature Phys.* **12** (5), 465–468 (2016) .
8. Shaniv, R. *et al.* New methods for testing Lorentz invariance with atomic systems. *Phys. Rev. Lett.* **120**, 103202 (2018) .
9. Mattingly, D. Modern tests of Lorentz invariance. *Living Rev. Relativ.* **8** (2005). <https://doi.org/https://doi.org/10.12942/lrr-2005-5> .
10. Hořava, P. Quantum gravity at a Lifshitz point. *Phys. Rev. D* **79**, 084008 (2009). URL <https://link.aps.org/doi/10.1103/PhysRevD.79.084008>. <https://doi.org/10.1103/PhysRevD.79.084008> .

11. Pospelov, M. & Shang, Y. Lorentz violation in Hořava-Lifshitz-type theories. *Phys. Rev. D* **85**, 105001 (2012). URL <https://link.aps.org/doi/10.1103/PhysRevD.85.105001>. <https://doi.org/10.1103/PhysRevD.85.105001> .
12. Tobar, M. E., Wolf, P., Bize, S., Santarelli, G. & Flambaum, V. Testing local Lorentz and position invariance and variation of fundamental constants by searching the derivative of the comparison frequency between a cryogenic sapphire oscillator and hydrogen maser. *Phys. Rev. D* **81**, 022003 (2010). URL <https://link.aps.org/doi/10.1103/PhysRevD.81.022003>. <https://doi.org/10.1103/PhysRevD.81.022003> .
13. Kostelecký, V. A. & Potting, R. *CPT*, strings, and meson factories. *Phys. Rev. D* **51**, 3923–3935 (1995). URL <https://link.aps.org/doi/10.1103/PhysRevD.51.3923>. <https://doi.org/10.1103/PhysRevD.51.3923> .
14. Liberati, S. & Mattingly, D. Lorentz breaking effective field theory models for matter and gravity: theory and observational constraints. *arXiv:1208.1071 [gr-qc]* (2012) .
15. Abazov, V. M. *et al.* Search for violation of Lorentz invariance in top quark pair production and decay. *Phys. Rev. Lett.* **108**, 261603 (2012). URL <https://link.aps.org/doi/10.1103/PhysRevLett.108.261603>. <https://doi.org/10.1103/PhysRevLett.108.261603> .
16. Aaij, R. *et al.* Search for violations of Lorentz invariance and *CPT* symmetry in $B_{(s)}^0$ mixing. *Phys. Rev. Lett.* **116**, 241601 (2016). URL <https://link.aps.org/doi/10.1103/PhysRevLett.116.241601>. <https://doi.org/10.1103/PhysRevLett.116.241601> .
17. Albert, A. *et al.* Constraints on Lorentz invariance violation from HAWC observations of gamma rays above 100 TeV. *Phys. Rev. Lett.* **124**, 131101 (2020). URL <https://link.aps.org/doi/10.1103/PhysRevLett.124.131101>. <https://doi.org/10.1103/PhysRevLett.124.131101> .
18. Michelson, A. A. & Morley, E. W. Influence of motion of the medium on the velocity of light. *Am. J. Science* **34** (1887) .
19. Herrmann, S. *et al.* Rotating optical cavity experiment testing Lorentz invariance at the 10^{-17} level. *Phys. Rev. D* **80**, 105011 (2009). URL <https://link.aps.org/doi/10.1103/PhysRevD.80.105011>. <https://doi.org/10.1103/PhysRevD.80.105011> .
20. Müller, H., Herrmann, S., Braxmaier, C., Schiller, S. & Peters, A. Modern Michelson-Morley experiment using cryogenic optical resonators. *Phys. Rev. Lett.* **91**, 020401 (2003). URL <https://link.aps.org/doi/10.1103/PhysRevLett.91.020401>. <https://doi.org/10.1103/PhysRevLett.91.020401> .
21. Eisele, C., Nevsky, A. Y. & Schiller, S. Laboratory test of the isotropy of light propagation at the 10^{-17} level. *Phys. Rev. Lett.* **103**, 090401 (2009). URL <https://link.aps.org/doi/10.1103/PhysRevLett.103.090401>. <https://doi.org/10.1103/PhysRevLett.103.090401> .
22. Safronova, M. S. *et al.* Search for new physics with atoms and molecules. *Rev. Mod. Phys.* **90**, 025008 (2018). URL <https://link.aps.org/doi/10.1103/RevModPhys.90.025008>. <https://doi.org/10.1103/RevModPhys.90.025008> .

23. Hughes, V. W., Robinson, H. G. & Beltran-Lopez, V. Upper limit for the anisotropy of inertial mass from nuclear resonance experiments. *Phys. Rev. Lett.* **4**, 342–344 (1960). URL <https://link.aps.org/doi/10.1103/PhysRevLett.4.342>. <https://doi.org/10.1103/PhysRevLett.4.342> .
24. Brown, J. M., Smullin, S. J., Kornack, T. W. & Romalis, M. V. New limit on Lorentz- and *CPT*-violating neutron spin interactions. *Phys. Rev. Lett.* **105**, 151604 (2010). URL <https://link.aps.org/doi/10.1103/PhysRevLett.105.151604>. <https://doi.org/10.1103/PhysRevLett.105.151604> .
25. Smiciklas, M., Brown, J. M., Cheuk, L. W., Smullin, S. J. & Romalis, M. V. New test of local Lorentz invariance using a ^{21}Ne – Rb – K comagnetometer. *Phys. Rev. Lett.* **107**, 171604 (2011). URL <https://link.aps.org/doi/10.1103/PhysRevLett.107.171604>. <https://doi.org/10.1103/PhysRevLett.107.171604> .
26. Lange, R. *et al.* Lifetime of the $^2F_{7/2}$ level in Yb^+ for spontaneous emission of electric octupole radiation. *Phys. Rev. Lett.* **127**, 213001 (2021). URL <https://link.aps.org/doi/10.1103/PhysRevLett.127.213001>. <https://doi.org/10.1103/PhysRevLett.127.213001> .
27. Genov, G. T., Schraft, D., Vitanov, N. V. & Halfmann, T. Arbitrarily accurate pulse sequences for robust dynamical decoupling. *Phys. Rev. Lett.* **118**, 133202 (2017). URL <https://link.aps.org/doi/10.1103/PhysRevLett.118.133202>. <https://doi.org/10.1103/PhysRevLett.118.133202> .
28. Colladay, D. & Kostelecký, V. A. Lorentz-violating extension of the standard model. *Phys. Rev. D* **58**, 116002 (1998). URL <https://link.aps.org/doi/10.1103/PhysRevD.58.116002>. <https://doi.org/10.1103/PhysRevD.58.116002> .
29. Kostelecký, V. A. & Russell, N. Data tables for Lorentz and *CPT* violation. *Rev. Mod. Phys.* **83**, 11–31 (2011). URL <https://link.aps.org/doi/10.1103/RevModPhys.83.11>. <https://doi.org/10.1103/RevModPhys.83.11> .
30. Furst, H. A. *et al.* Coherent excitation of the highly forbidden electric octupole transition in $^{172}\text{Yb}^+$. *Phys. Rev. Lett.* **125**, 163001 (2020). URL <https://link.aps.org/doi/10.1103/PhysRevLett.125.163001>. <https://doi.org/10.1103/PhysRevLett.125.163001> .
31. Zhang, W. *et al.* Ultrastable silicon cavity in a continuously operating closed-cycle cryostat at 4 K. *Phys. Rev. Lett.* **119**, 243601 (2017). URL <https://link.aps.org/doi/10.1103/PhysRevLett.119.243601>. <https://doi.org/10.1103/PhysRevLett.119.243601> .
32. Huntemann, N., Sanner, C., Lipphardt, B., Tamm, C. & Peik, E. Single-ion atomic clock with 3×10^{-18} systematic uncertainty. *Phys. Rev. Lett.* **116**, 063001 (2016). URL <https://link.aps.org/doi/10.1103/PhysRevLett.116.063001>. <https://doi.org/10.1103/PhysRevLett.116.063001> .
33. Lange, R. *et al.* Coherent suppression of tensor frequency shifts through magnetic field rotation. *Phys. Rev. Lett.* **125**, 143201 (2020). URL <https://link.aps.org/doi/10.1103/PhysRevLett.125.143201>. <https://doi.org/10.1103/PhysRevLett.125.143201> .

34. Ludlow, A. D., Boyd, M. M., Ye, J., Peik, E. & Schmidt, P. O. Optical atomic clocks. *Rev. Mod. Phys.* **87**, 637–701 (2015). URL <https://link.aps.org/doi/10.1103/RevModPhys.87.637>. <https://doi.org/10.1103/RevModPhys.87.637> .
35. Glynn, E. F., Chen, J. & Mushegian, A. R. Detecting periodic patterns in unevenly spaced gene expression time series using Lomb–Scargle periodograms. *Bioinformatics* **22** (3), 310–316 (2005). URL <https://doi.org/10.1093/bioinformatics/bti789>, <https://arxiv.org/abs/https://academic.oup.com/bioinformatics/article-pdf/22/3/310/18529532/bti789.pdf> .
36. Kostecký, V. A. & Vargas, A. J. Lorentz and *CPT* tests with clock-comparison experiments. *Phys. Rev. D* **98**, 036003 (2018). URL <https://link.aps.org/doi/10.1103/PhysRevD.98.036003>. <https://doi.org/10.1103/PhysRevD.98.036003> .
37. Vargas, A. J. Overview of the phenomenology of Lorentz and *CPT* violation in atomic systems. *Symmetry* **11** (12) (2019). URL <https://www.mdpi.com/2073-8994/11/12/1433>. <https://doi.org/10.3390/sym11121433> .
38. Morigi, G., Eschner, J. & Keitel, C. H. Ground state laser cooling using electromagnetically induced transparency. *Phys. Rev. Lett.* **85**, 4458–4461 (2000). URL <https://link.aps.org/doi/10.1103/PhysRevLett.85.4458>. <https://doi.org/10.1103/PhysRevLett.85.4458> .
39. Ejtemaee, S. & Haljan, P. C. 3D Sisyphus cooling of trapped ions. *Phys. Rev. Lett.* **119**, 043001 (2017). URL <https://link.aps.org/doi/10.1103/PhysRevLett.119.043001>. <https://doi.org/10.1103/PhysRevLett.119.043001> .
40. Joshi, M. K. *et al.* Polarization-gradient cooling of 1D and 2D ion Coulomb crystals. *New Journal of Physics* **22** (10), 103013 (2020). URL <https://doi.org/10.1088/1367-2630/abb912>. <https://doi.org/10.1088/1367-2630/abb912> .
41. Pyka, K., Herschbach, N., Keller, J. & Mehlstäubler, T. E. A high-precision segmented Paul trap with minimized micromotion for an optical multiple-ion clock. *Appl. Phys. B* **114** (1), 231–241 (2014). <https://doi.org/https://doi.org/10.1007/s00340-013-5580-5> .
42. Keller, J. *et al.* Probing time dilation in Coulomb crystals in a high-precision ion trap. *Phys. Rev. Applied* **11**, 011002 (2019). URL <https://link.aps.org/doi/10.1103/PhysRevApplied.11.011002>. <https://doi.org/10.1103/PhysRevApplied.11.011002> .
43. Keller, J., Partner, H. L., Burgermeister, T. & Mehlstäubler, T. E. Precise determination of micromotion for trapped-ion optical clocks. *Journal of Applied Physics* **118** (10), 104501 (2015). <https://doi.org/10.1063/1.4930037> .
44. Pyka, K. *High-precision ion trap for spectroscopy of Coulomb crystals*. Ph.D. thesis, Leibniz Universität Hannover, Welfengarten 1, 30167, Hanover, Germany (2013).
45. Kalincev, D. *et al.* Motional heating of spatially extended ion crystals. *Quantum Science and Technology* **6** (3), 034003 (2021). URL <https://doi.org/10.1088/2058-9565/abec99>. <https://doi.org/10.1088/2058-9565/abec99> .

46. Roos, C. F., Chwalla, M., Kim, K., Riebe, M. & Blatt, R. Precision spectroscopy with entangled states: Measurement of electric quadrupole moments. *AIP Conference Proceedings* **869** (1), 111–118 (2006). URL <https://aip.scitation.org/doi/abs/10.1063/1.2400640>. <https://doi.org/10.1063/1.2400640>, <https://arxiv.org/abs/https://aip.scitation.org/doi/pdf/10.1063/1.2400640> .

Acknowledgments. We thank Melina Filzinger, Richard Lange, Burkhard Lipphardt, Nils Huntemann and Andre Kulosa for experimental support. We thank Ralf Lehnert, Arnaldo Vargas, Nils Huntemann and Ekkehard Peik for helpful discussions. We thank Ralf Lehnert for carefully reading the manuscript.

Funding L.S.D. acknowledges support from the Alexander von Humboldt foundation. This project has been funded by the Deutsche Forschungsgemeinschaft (DFG, German Research Foundation) under Germany’s Excellence Strategy – EXC-2123 QuantumFrontiers –390837967 (RU B06) and through Grant No. CRC 1227 (DQ-mat, project B03). This work has been supported by the Max-Planck-RIKEN-PTB-Center for Time, Constants and Fundamental Symmetries.

Conflict of interest/Competing interests The authors declare that they have no competing interests.

Authors’ contributions Conception of the experiment and development of methods: L.S.D., C-H.Y., H.A.F., K.C.G., T.E.M. Design and construction of experimental apparatus: L.S.D., C-H.Y., H.A.F., T.E.M. Data acquisition and analysis: L.S.D., C-H.Y. Preparation and discussion of the manuscript: L.S.D., C-H.Y., H.A.F., K.C.G., T.E.M.